Geophysical and Astrophysical Fluid Dynamics
Vol. 98, No. 3, June 2004, pp. 241–255

Taylor & Francis
Taylor & Francis Group

2D STUDIES OF VARIOUS APPROXIMATIONS USED FOR MODELING CONVECTION IN GIANT PLANETS

MARTHA EVONUK* and GARY A. GLATZMAIER

Department of Earth Sciences, University of California, Santa Cruz, CA, 95064 USA

(Received 23 August 2003; In final form 13 January 2004)

The effects of common approximations made when modeling convection in the interior of giant planets, like Jupiter, are examined using two-dimensional (2D) numerical calculations at high Rayleigh number (10^{10}). Small scale flow structures along the upper boundary and large scales in the lower region are observed for an anelastic fluid spanning five density scale heights. A much more symmetric distribution in the scale of flow structures is observed for a Boussinesq fluid in which density stratification is neglected. The absence of magnetic fields results in higher fluid velocities and smaller scale flow structures. Neglecting the inertial terms produces narrower plumes and a fundamentally different fluid flow pattern for anelastic fluids. Although restricted to two dimensions, our results demonstrate that the spatial structure and time dependence of thermal convection are significantly influenced by density stratification, magnetic fields and inertia. These effects should not be ignored in three-dimensional (3D) convection models of giant planets.

Keywords: Giant plants; Numerical modeling

1 INTRODUCTION

Approximations, such as assuming constant density and neglecting magnetic fields and inertial terms, are often used when modeling convection in the interior of giant planets like Jupiter. Models with these approximations, however, may not accurately capture the fluid dynamics within these giant planets. For example, giant gaseous planets experience a significant change in density with depth (Guillot, 1999). Models that assume a constant background density profile, the Boussinesq approximation, are approximately valid only for very thin shells within a giant planet. However, deep interior models of Jupiter have employed the Boussinesq approximation (e.g., Sun *et al.*, 1993; Aurnou and Olson, 2001; Christensen, 2001, 2002; Wicht *et al.*, 2002).

Shock pressure experiments suggest that hydrogen in Jupiter should become metallic at roughly 1.4 Mbars (Nellis *et al.*, 1996) which corresponds to about 0.84 of Jupiter's radius (Guillot, 1999). Convection of this electrically-conducting hydrogen in the deep

*Corresponding author. E-mail: mevonuk@emerald.ucsc.edu

ISSN 0309-1929 print: ISSN 1029-0419 online
DOI: 10.1080/03091920410001696126

interior of Jupiter, under the influence of planetary rotation, maintains Jupiter's magnetic field. The resulting strong Lorentz forces on the fluid may significantly influence the convective structure; however most models of Jupiter neglect magnetic fields.

Neglecting the inertial terms is a common practice when modeling convection in the Earth's mantle (e.g., Tackley *et al.*, 1993; Bunge *et al.*, 1996). Several models for the geodynamo also neglect part or all of the inertial term (e.g., Glatzmaier and Roberts, 1995; Kuang and Bloxham, 1999). If we look at the ratio of inertial to Coriolis terms, the Rossby Number, we get roughly 10^{-13} for the Earth's mantle, 10^{-7} for the Earth's liquid core, and 10^{-2} for Jupiter's interior. Therefore neglecting the inertial terms is a good approximation for mantle convection and a relatively good approximation for the geodynamo; but it is a poor approximation for Jupiter. Neglecting inertial terms is usually justified when the ratio of viscous to thermal diffusivities, the Prandtl number, is very large (see (14) below), as it is for the Earth's mantle; but again, this is not the case for Jupiter.

In order to look at the effects of these approximations in closer detail, seven model cases were examined using two-dimensional (2D) numerical calculations at high Rayleigh number (10^{10}). The cases consisted of constant density and stratified density profiles with rotation and magnetic fields, with magnetic fields but without rotation, without magnetic fields, and without inertial terms.

2 NUMERICAL MODEL

We numerically simulate 2D thermal convection in a rotating, electrically-conducting fluid with flow and field in the x–z plane. Two density profiles are considered: a Boussinesq profile with no density stratification, and therefore no rotational effects, and an anelastic profile spanning five density scale heights ($N_\rho = 5$), making the fluid at the bottom 148 times as dense as the fluid at the top. In all other aspects these two calculations are the same. Calculations with each density profile are then simplified by excluding first the rotational terms for the anelastic case, then the magnetic fields, and finally the inertial terms.

The governing equations for perturbations relative to an adiabatic, hydrostatic, rotating reference state are the momentum equation (1), the heat equation (2), the magnetic induction equation (3), and the equations governing the conservation of mass (4) and magnetic flux (5) are

$$\frac{\partial \mathbf{v}}{\partial t} = -(\mathbf{v}\cdot\nabla)\mathbf{v} - \nabla p + \nu\left(\nabla^2\mathbf{v} + \frac{1}{3}\nabla(\nabla\cdot\mathbf{v})\right) + \frac{g_o}{C_p}S\hat{\mathbf{z}} + 2\mathbf{v}\times\boldsymbol{\Omega} + \frac{1}{\bar{\rho}}(\mathbf{J}\times\mathbf{B}), \tag{1}$$

$$\frac{\partial S}{\partial t} = -(\mathbf{v}\cdot\nabla)S + \kappa\left(\nabla^2 S + \frac{d}{dz}\ln(\bar{\rho}\bar{T})\frac{\partial S}{\partial z}\right), \tag{2}$$

$$\frac{\partial \mathbf{B}}{\partial t} = \nabla\times(\mathbf{v}\times\mathbf{B}) + \eta\nabla^2\mathbf{B}, \tag{3}$$

$$\nabla\cdot(\bar{\rho}\mathbf{v}) = 0, \tag{4}$$

$$\nabla\cdot\mathbf{B} = 0. \tag{5}$$

Here $\mathbf{v}$ is the velocity vector, S is the specific entropy perturbation, $\mathbf{B}$ is the magnetic field, $\mathbf{J} = \mu^{-1}\nabla\times\mathbf{B}$ is the electric current density, $\bar{\rho}$ is the reference state density (a function of depth), and p is the sum of the pressure perturbation divided by $\bar{\rho}$ and the gravitational potential perturbation (Braginsky and Roberts, 1995). We assume the viscous, ν, thermal, κ, and magnetic, η, diffusivities are constants, as are the specific heat capacity at constant pressure, C_p, the magnetic permeability, μ, the gravitational acceleration, g_o, in the $-z$ direction and the angular velocity, $\mathbf{\Omega}$, of the rotating frame. For these calculations we choose $\mathbf{\Omega}$ to be negative, i.e. in the $-$y direction. Since we are interested in turbulent convection in the deep interiors of giant planets, ν and κ are considered turbulent diffusivities and the diffusive heat flux in equation (2) has been set proportional to the entropy gradient (Braginsky and Roberts, 1995). The momentum equation (1) has been simplified by dropping the additional viscous diffusion terms that would depend on the density gradient if ν were a molecular viscosity. In addition, viscous and ohmic heating have been neglected in the heat equation (2) for these high Rayleigh number, low diffusion, simulations.

We assume a polytropic reference state to determine the relationship between $\bar{\rho}$ and N_ρ, the number of density scale heights, in the following two equations (6) and (7) where z indicates the height, ρ_o is the reference state density at the lower boundary, z_o is the stratification parameter, and n is the polytropic index:

$$N_\rho = -n\ln\left(1-\frac{D}{z_o}\right), \tag{6}$$

$$\bar{\rho}(z) = \rho_o\left(1-\frac{z}{z_o}\right)^n. \tag{7}$$

We choose the adiabatic reference state to be

$$T(z) = T_o\left(1-\frac{z}{z_o}\right), \tag{8}$$

as it would be for a polytropic perfect gas. The Boussinesq limit is reached as $z_o\to\infty$ and the strongly stratified limit as $z_o\to D$, where D is the depth of the box in z direction. The polytropic index, n, is set to 0.95 for the deep interior of Jupiter (Hubbard, 1984).

The upper and lower boundaries of the box are impermeable, stress-free (free-slip), and are set to a constant value of entropy. The side boundaries are periodic. The length of the box in the x direction is L, so the aspect ratio is $a = L/D$. A uniform background magnetic field with amplitude B_o is applied in the z direction. The total magnetic flux (per unit length in the y direction) through any z level is constrained to be B_oL.

The governing dimensionless parameters are the Rayleigh number, $Ra = g_o\Delta S D^3/\nu\kappa C_p = 10^{10}$, the Prandtl number, $Pr = \nu/\kappa = 1$ or ∞, the Ekman number, $Ek = \nu/2|\Omega|D^2 = 10^{-5}$ or ∞, the Roberts number, $q = \kappa/\eta = 1$, and the

Chandrasekhar number, $Q = B_o^2 D^2/\rho\nu\mu\eta = 10^4$ or 0. Here ΔS is the specified drop in specific entropy across the box and ρ is the reference state density in the middle of the box. For $Pr = 1$, $Ek = 10^{-5}$, and $Ra = 10^{10}$ the convective Rossby number, $Ro = (RaEk^2/Pr)^{1/2} = (g_o \Delta S/4\Omega^2 DC_p)^{1/2}$, is 1.0, meaning the Coriolis and buoyancy forces should be roughly comparable.

We use the vorticity-stream-function method (Weiss, 1981a) where the curl of the momentum equation is written in terms of the vorticity, $\boldsymbol{\omega} = \nabla \times \mathbf{v}$. The stream function, $\boldsymbol{\Psi}$, for our anelastic model is defined such that the mass flux $\bar{\rho}\mathbf{v} = \nabla \times \boldsymbol{\Psi}$. In this 2D model, $\boldsymbol{\omega}$ and $\boldsymbol{\Psi}$ are in the y direction. Their amplitudes, ω and Ψ, are related by

$$\omega = -\frac{1}{\bar{\rho}}\left[\nabla^2 \Psi - h_\rho \frac{\partial \Psi}{\partial z}\right] \tag{9}$$

with

$$v_x = -\frac{1}{\bar{\rho}}\frac{\partial \Psi}{\partial z}, \qquad v_z = \frac{1}{\bar{\rho}}\frac{\partial \Psi}{\partial x} \tag{10}$$

and

$$h_\rho = \frac{1}{\bar{\rho}}\frac{d\bar{\rho}}{dz} = \frac{-n}{z_o - z}. \tag{11}$$

The magnetic induction equation is written in terms of the vector potential, $\mathbf{A}$ such that $\mathbf{B} = \nabla \times \mathbf{A}$; we choose the Coulomb gauge, $\nabla \cdot \mathbf{A} = 0$. In 2D, $\mathbf{A}$ and $\mathbf{J}$ are in the y direction. Their amplitudes, A and J, are related by

$$J = -\frac{1}{\mu}\nabla^2 A \tag{12}$$

with

$$B_x = -\frac{\partial A}{\partial z} \quad \text{and} \quad B_z = \frac{\partial A}{\partial x}. \tag{13}$$

After scaling length by D, time by D^2/κ, entropy by ΔS, magnetic field by B_o and density by ρ_o, the resulting nondimensional, anelastic equations are

$$\frac{\partial \omega}{\partial t} = -(\mathbf{v}\cdot\nabla)\omega + h_\rho \omega v_z - RaPr\frac{\partial S}{\partial x} + Pr\nabla^2\omega + \frac{QPr}{q\bar{\rho}}[\nabla\cdot(J\mathbf{B}) - h_\rho J B_z] - Ek^{-1}Prh_\rho v_z, \tag{14}$$

$$\frac{\partial S}{\partial t} = -(\mathbf{v}\cdot\nabla)S + \nabla^2 S + (h_\rho + h_T)\frac{\partial S}{\partial z}, \tag{15}$$

$$\frac{\partial A}{\partial t} = -(\mathbf{v}\cdot\nabla)A + \frac{1}{q}\nabla^2 A, \tag{16}$$

where

$$h_T = \frac{1}{\bar{T}}\frac{d\bar{T}}{dz} = -\frac{1}{z_o - z}. \tag{17}$$

The numerical technique consists of a spectral method in the horizontal direction with 200 complex Fourier modes and finite differencing in the vertical direction on a Chebyshev grid with 600 levels. The Chebyshev grid naturally provides greater resolution near the boundaries where it is needed. The Fourier expansion for a variable, f, is

$$\begin{aligned} f(x, z, t) &= \sum_{m=-M}^{M} f_m(z, t) \exp(ik_m x) \\ &= f_o(z, t) + 2\sum_{m=1}^{M} \text{Real}[f_m(z, t) \exp(ik_m x)] \end{aligned} \tag{18}$$

where M is the truncation degree and $k_m = 2\pi m/a$. The vector potential, A, has an additional term, x, outside the summation that represents the uniform, vertical, background magnetic field, scaled by B_o.

This type of expansion allows for periodic boundary conditions at the side boundaries. Boundary conditions on the top and bottom borders are: $S_{m>0} = \partial A_m/\partial z = \Psi_m = (\partial^2\Psi_m/\partial z^2 - h_\rho(\partial\Psi_m/\partial z)) = 0$ and therefore $\omega_m = 0$. At the bottom boundary ($z = 0$), $S_o = 1$ and at the top boundary ($z = 1$), $S_o = 0$.

The prognostic equations (14)–(16) are evolved in time using an implicit Crank–Nicolson scheme for the linear terms and an explicit Adams–Bashforth scheme for the nonlinear terms. A spectral transform method is employed to calculate the nonlinear terms.

The 2D box is oriented so as to represent convection on the equatorial plane of the planet. This allows for the addition of the rotational term with the axis of rotation perpendicular to the plane of the box. Counter-clockwise rotation of the box, with the axis of rotation out of the page, causes the expanding fluid to spin clockwise and contracting fluid to spin counter-clockwise (Glatzmaier and Gilman, 1981). In 2D Cartesian geometry, the Coriolis forces are totally balanced by part of the pressure field in the Boussinesq limit. That is, there is no vorticity generation due to Coriolis effects when the reference state density is constant (i.e., $h_\rho = 0$ in (14)). Only our anelastic cases are influenced by rotation. Rotating convection in three dimensions (3D) certainly feels the effects of Coriolis forces (i.e., Julien *et al.*, 1996), but that flow structure would of course not be present in our 2D simulation.

3 RESULTS

We first compare the various cases in this study by visual inspection of snapshots of the entropy field. Then we compare the entropy fields using the vertical profile of the mean in time and horizontal dimension, $\mu_s = \langle S \rangle$, the standard deviation, $\sigma_s^{1/2} = \langle [S - \langle S \rangle]^2 \rangle^{1/2}$, the flatness, $F_s = \langle [S - \langle S \rangle]^4 \rangle / \sigma_s^2$, and the skewness, $s_s = \langle [S - \langle S \rangle]^3 \rangle / \sigma_s^{3/2}$. In addition, the root mean square (RMS) velocity in the horizontal direction, $\sigma_x^{1/2} = \langle [v_x - \langle v_x \rangle]^2 \rangle^{1/2}$, and in the vertical direction, $\sigma_z^{1/2} = \langle [v_z - \langle v_z \rangle]^2 \rangle^{1/2}$, the skewness of

the vertical velocity, $s_z = \langle [v_z - \langle v_z \rangle]^3 \rangle / \sigma_z^{3/2}$, and the skewness of the vorticity, $s_\omega = \langle [\omega - \langle \omega \rangle]^3 \rangle / \langle [\omega - \langle \omega \rangle]^2 \rangle^{3/2}$ are examined. Another measure of how the various simplifications examined here affect the solution is provided by probability density functions (PDFs) for the entropy and vorticity. We approximate the PDF for a variable by measuring the relative frequency of its normalized deviation from the average in time and x for a given range in z.

A visual examination of the resulting entropy fields, shown in Fig. 1 for three of the anelastic cases (rotation and magnetic field, without rotation or magnetic field, and without inertial terms) and a Boussinesq case (inertial without magnetic fields) easily

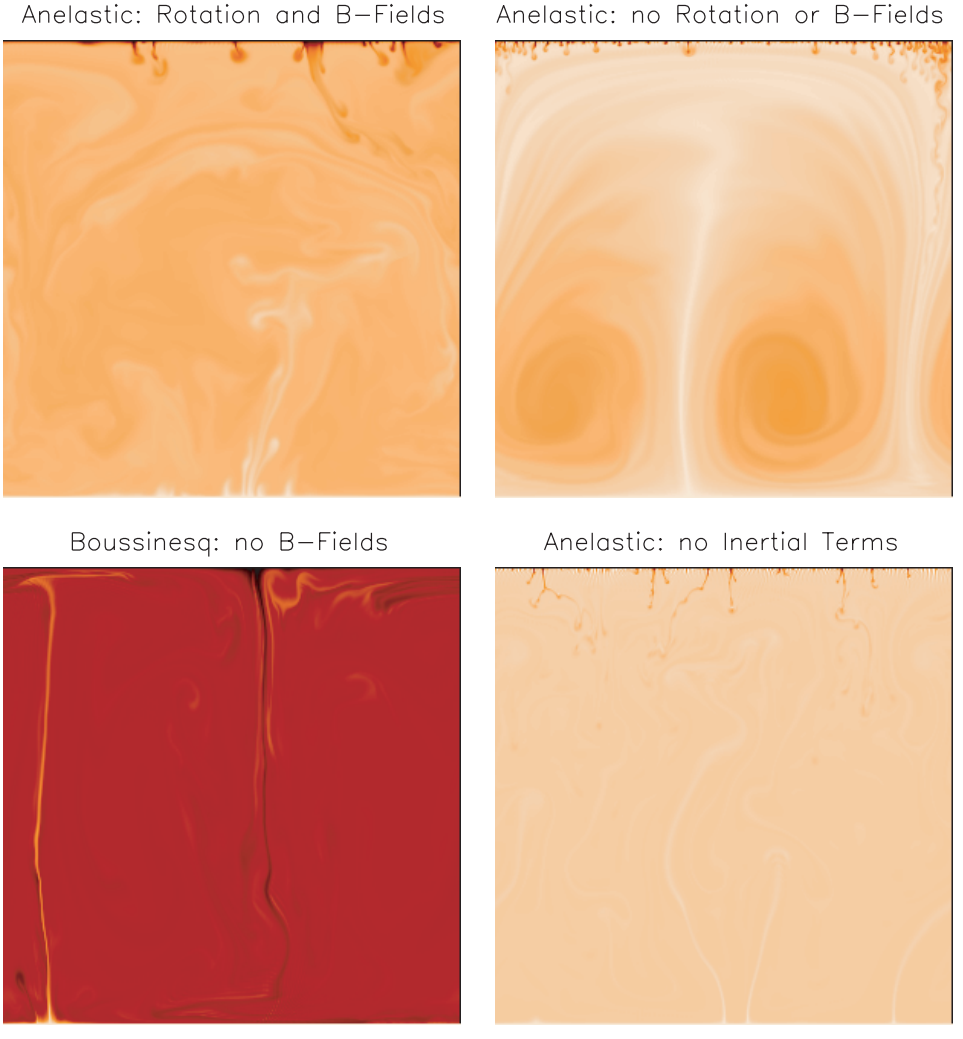

FIGURE 1 Snapshots of the entropy field showing three anelastic cases and one Boussinesq case. The anelastic cases are with rotation and magnetic fields (upper left), without rotation or magnetic fields (upper right) and without inertial terms (lower right). The Boussinesq case shown is inertial without magnetic fields (lower left). High entropy is represented by lighter shades of red and low entropy is represented by darker shades of red. These snapshots are typical of the solutions seen in these cases.

TABLE I The standard deviation of ω^2 relative to its mean over 100 000 time steps and 360 000 grid points

	Nonmagnetic	*Magnetic*	*Noninertial*
Boussinesq	9.41×10^{-3}	4.41×10^{-2}	1.95×10^{-1}
Anelastic	1.30×10^{-2}	6.58×10^{-2}	1.24×10^{-1}

demonstrates that there are differences in the fluid behavior and the size, shape and abundance of thermal plumes. Horizontal fluid motion causes the magnetic field lines to converge where plumes develop, as seen in earlier Boussinesq simulations at much lower Rayleigh numbers (Weiss, 1981b). When the magnetic field is absent, smaller scale features are observed on the upper, low density boundary of the anelastic fluid, and along both the upper and lower boundaries of the Boussinesq fluid. The magnetic field, via the induction of electric current and the resulting Lorentz force, opposes fluid motion perpendicular to it; therefore without magnetic field to resist fluid flow, higher fluid velocities with smaller scale features develop. The temporal variability is also affected by the magnetic field. For example, the standard deviation of ω^2 divided by its mean over both time and space was greater in the cases with magnetic fields than in the cases without (Table I).

Removing the inertial terms, by using the infinite Prandtl number approximation, results in even finer scale structures, and larger, more time dependent fluid velocities. For these noninertial cases, the velocity solution at each time step needs to exactly balance, via the viscous term, all the other forces in the momentum equation. This typically requires more energy in the smallest resolved scales. Subsequently the velocity structure needs to adjust every time step without a history. For the inertial solutions however, the small scales of the net force determine the time rate of change of the small scale velocity and tend to average out over many time steps. Dropping the inertial terms also affects the temporal variation. This can be seen in the larger variation of ω^2 in the noninertial cases than in the inertial cases where the vorticity changes more slowly as forces are effectively time-averaged (Table I). While the noninertial Boussinesq case manages to maintain a convection cell with a single upwelling and down-welling plume, the noninertial anelastic case loses its one cell convective behavior opting for several rising and sinking plumes that do not span the vertical extent of the box.

The large density stratification in the anelastic cases results in the bulk of the mass being restricted to the lower regions of the simulation. This causes an effective increase of the aspect ratio as the center of the circulation of material is shifted downward with respect to the Boussinesq cases. This effect is also seen in 2D fully compressible simulations where the density stratification was varied (Hurlburt *et al.*, 1984).

A more quantitative method of examining the model behavior is via the mean entropy profile, μ_s, and the standard deviation, $\sigma_s^{1/2}$, as functions of z (Fig. 2). The mean entropy profiles illustrate the division of turbulent convection into thin thermal boundary layers with steep entropy gradients that accelerate plumes away from the boundaries, and the bulk of the well mixed convection zone where the mean entropy gradient is small, that is, nearly adiabatic. The μ_s profiles of the three Boussinesq cases are identical and have a mean entropy in the bulk half way between the value for the top boundary and the bottom boundary. The standard deviation from this mean is also symmetric with respect to mid-depth, and peaks in the boundary layers. These Boussinesq profiles are similar to those seen for low Rayleigh number 3D,

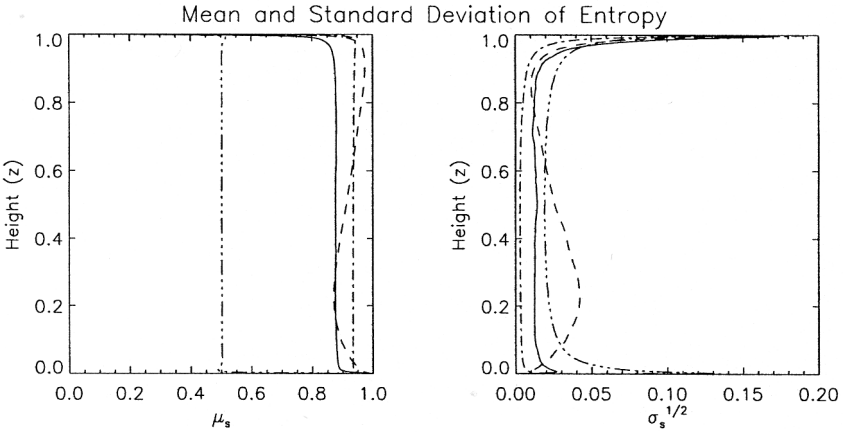

FIGURE 2 The mean and standard deviation of the entropy with height in the simulation is shown for anelastic with rotation and magnetic fields (solid line), anelastic without rotation or magnetic fields (dashed line), anelastic without inertial terms (dash single dot line), and Boussinesq with magnetic fields (dash triple dot line).

periodic, Boussinesq studies (Sirovich *et al.*, 1989; Kerr, 1996), however our higher Rayleigh number causes the thermal boundary layers to be much thinner. Notice, however, how the mean entropy in the bulk is significantly higher for the anelastic cases and the standard deviation is relatively small near the bottom boundary and large near the top.

Density stratification is responsible for these anisotropic profiles for the anelastic cases. The diffusive heat fluxes through the bottom and top boundaries are, on average, the same and equal to $-\bar{\rho}\bar{T}\kappa\partial S/\partial z$. Since $\bar{\rho}\bar{T}$ is much greater at the bottom boundary, $|\partial S/\partial z|$ needs to be much greater at the top boundary. Since the depth of the thermal boundary layers are comparable, there is a larger drop in entropy across the top thermal boundary layer and therefore a mean entropy is greater than 0.5 in the bulk of the convection zone. The standard deviation vanishes at the boundaries because of our boundary conditions and peaks within the thermal boundary layers because of the intense, small scale plumes that develop there. These plumes develop from the boundary layer instabilities driven by the large superadiabatic temperature gradients. Large scale horizontal winds, at both boundaries, sweep the small scale plumes into larger scale plumes.

The nonmagnetic, nonrotating anelastic case displays subadiabatic behavior that is very pronounced. These sinuous μ_s and $\sigma_s^{1/2}$ profiles, indicate the presence of over-shooting thermal plumes. Cold sinking plumes are not able to heat up fast enough and therefore over cool the lower region before hitting the lower boundary. Likewise, hot, rising plumes over heat the upper regions. All the thermal driving occurs in the shallow thermal boundary layers as the plumes get shot out and then coast through the bulk of the convection zone to the other side. In the cases examined here, Coriolis and Lorentz forces produce a more adiabatic mean in the bulk, suppressing the over-shooting of thermal plumes and deviations from the mean entropy.

The flatness of the entropy, F_s, indicates how peaked a PDF is relative to a normal distribution; a pure Gaussian has a flatness of 3, whereas a pure exponential has a flatness of 6. High values of flatness correspond to a more distinct peak in the PDF

near the mean whereas low values of flatness correspond to a PDF with a flatter top near the mean. A uniform distribution would be the extreme case of low F_s. In the original hard turbulence experiment of Heslot *et al.* (1987), PDFs of temperature in the central plane changed from Gaussian to exponential as the Nusselt–Rayleigh number power law scale changed from its soft turbulent value of 1/3 to its hard turbulent value of 2/7. Simulations by Kerr (1996) at various Rayleigh numbers from 5×10^4 to 2×10^7 show the beginning of the transition to exponential ($F_s \simeq 4.5$) for 3D Boussinesq runs. Exponential PDFs in 2D were seen for both soft and hard turbulence by DeLuca *et al.* (1990) for Rayleigh numbers between 1.9×10^6 and 1.6×10^8. They determined that the appearance of the exponential form was purely diagnostic of the presence of plumes within the flow and not a transition to the hard turbulent state.

Vertical profiles of flatness for four of our cases are plotted in Fig. 3. PDF profiles of entropy for the nonmagnetic Boussinesq case and the magnetic rotating anelastic case are displayed in Fig. 4 at various ranges of depth in the fluid: $0.0 \leq z \leq 0.083$, $0.125 \leq z \leq 0.292$, $0.375 \leq z \leq 0.625$, $0.708 \leq z \leq 0.875$, and $0.917 \leq z \leq 1.0$. The magnetic Boussinesq case has large flatness values through its central regions in accordance with the sharp peaks in the PDFs. The inertial, anelastic cases have much lower F_s in their central regions which correspond to flatter distributions of the deviations of entropy from its mean. However, the two anelastic cases shown in Fig. 3 show different vertical distributions of flatness, as opposed to the Boussinesq cases which varied in magnitude but not shape. The magnetic, rotating anelastic case has comparable peaks in the flatness at the top and bottom boundaries while the noninertial case has values of flatness everywhere greater than the inertial cases and has a larger peak at the lower boundary.

The skewness of the entropy, s_s, (Fig. 5) can give insight into the nonsymmetry of the entropy PDFs shown in Fig. 4. The long tails to the right in the entropy PDFs

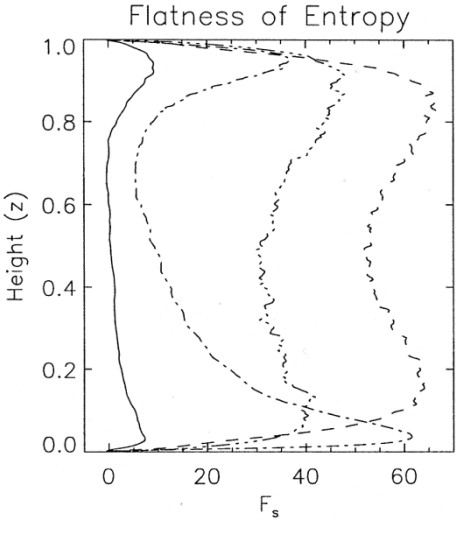

FIGURE 3 The flatness of the entropy with depth indicates how peaked the PDF is relative to a normal distribution. Cases shown here are the anelastic with rotation and magnetic fields (solid line), anelastic without inertial terms (dash single dot line), Boussinesq without inertial terms (dash triple dot line), and Boussinesq with magnetic fields (dashed line).

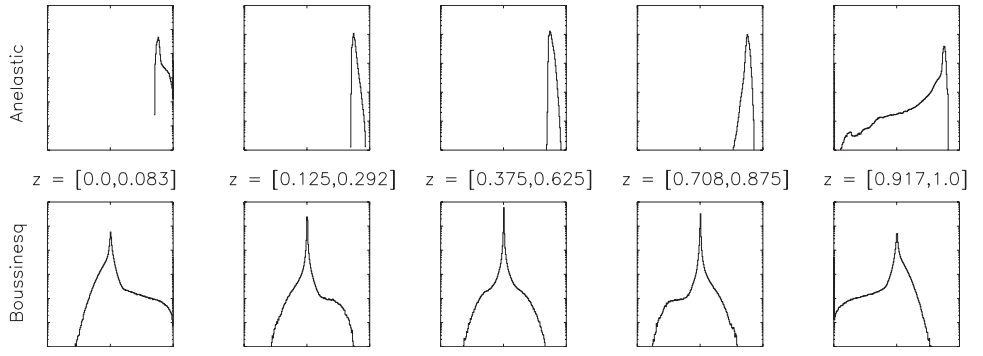

FIGURE 4 The probability density functions (PDFs) are shown here for anelastic with rotation and magnetic fields (top row) and Boussinesq with magnetic fields (bottom row). The PDFs are arranged by height from the bottom on the left to the top on the right. Specific ranges in z are shown between the two rows. The horizontal axis of each PDF corresponds to entropy with 0.0 on the left and 1.0 on the right. The vertical axis is on a log scale ranging from 10^1 to 10^7.

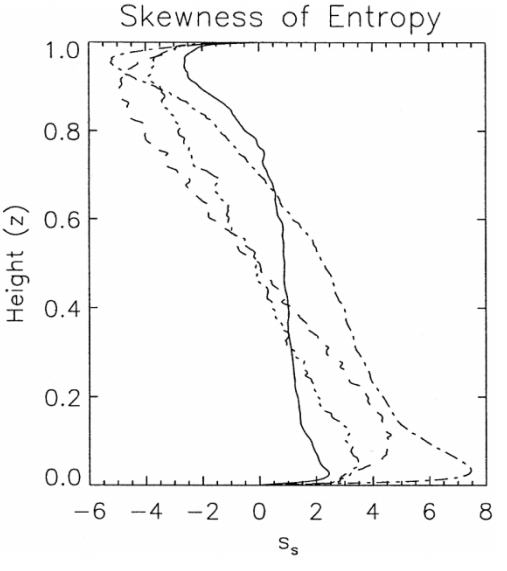

FIGURE 5 The skewness of entropy as a function of depth is shown here for anelastic with rotation and magnetic fields (solid line), anelastic without inertial terms (dash single dot line), Boussinesq without inertial terms (dash triple dot line), and Boussinesq with magnetic fields (dashed line).

correspond to positive skewness, tails to the left correspond to negative skewness, and symmetry to zero skewness. The entropy PDF (Fig. 4) is strongly peaked near the boundaries for the Boussinesq cases but has a long tail due to the influence of the boundary heating by small scale, hot plumes rising from the bottom boundary, and boundary cooling by small cold plumes sinking from the top boundary. This tail decreases in the intermediate region and is gone in the mid-plane. This structure for the Boussinesq case is also illustrated in Fig. 5 as a positive skewness in the bottom half and a negative skewness in the upper half. The anelastic cases have somewhat similar skewness profiles, but tend to reach symmetry much closer to the upper

boundary. This illustrates how the influence of the lower boundary has increased with the presence of a density stratification. The skewness peak near the upper boundary in the inertial anelastic cases, especially the nonrotating case, tends to have a greater magnitude than the skewness peak near the lower boundary as the transition from the high mean entropy of the midsection to the set boundary entropy value is more drastic at the upper boundary than at the lower boundary.

The RMS velocities of the fluids show how the bulk flow varies with depth. Figure 6 shows the vertical profiles of the RMS velocities in the horizontal direction, $\sigma_x^{1/2}$ and in the vertical direction, $\sigma_z^{1/2}$. Maximum values of the horizontal RMS near the boundaries indicates the presence of shear layers. Boundary shear layers are symmetric and much stronger in the Boussinesq cases, whereas for the inertial anelastic cases the shear flow near the bottom boundary is stronger than near the top, where the density scale height ($-h_\rho^{-1}$) is smallest. In the Boussinesq cases rising and sinking flows are symmetric, first forming small scale boundary-layer plumes which are then quickly swept into one large plume forming a single convection cell that spans the box and is vertically symmetric. In this relatively straight forward convection the vertical RMS velocity peaks at mid-depth where the horizontal RMS velocity is at its minimum.

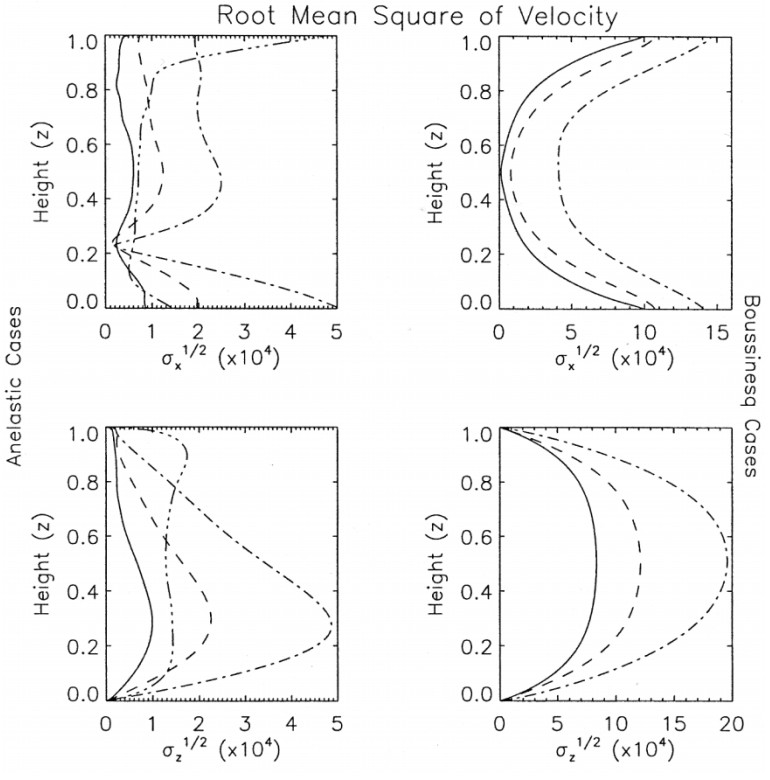

FIGURE 6 The RMS velocities of the fluids show the bulk flow patterns of the fluid with depth. The upper row shows the RMS of the horizontal velocity for the anelastic cases (left) and Boussinesq cases (right). The lower row shows the RMS of the vertical velocities for the same cases. Cases in the anelastic plots are magnetic with rotation (solid line), magnetic without rotation (dashed line), nonmagnetic and nonrotating (dashed single dot line), and noninertial (dashed triple dot line). Cases in the Boussinesq plots are magnetic (solid line), nonmagnetic (dashed line), and noninertial (dashed single dot line).

In the anelastic cases the density stratification causes rising material to expand and sinking material to contract which increases the effective aspect ratio since most of the mass is in the lower part of the box. Therefore, the maximum RMS vertical velocity and minimum RMS horizontal velocity occur closer to the bottom boundary. Most of the fluid rising from the dense lower region never comes close to the upper boundary because of the expansion. Plumes sinking from the top boundary quickly lose their identity because of the contraction. The noninertial anelastic case, however, shows a very different behavior; narrow sinking and rising plumes meet above the mid-plane with RMS vertical velocities nearly constant in height and relatively large RMS horizontal velocities near the top. In the cases examined here, RMS velocities are larger when there are no magnetic or Coriolis forces to resist the convective circulation.

By looking at the skewness of the vertical velocity, s_z, we can examine the fluid behavior in more detail (Fig. 7). A skewness of zero, as seen in the central regions of the Boussinesq cases, indicates an equal magnitude of rising and sinking material since the density is constant. In several past studies (Moeng and Rotunno, 1990; Kerr, 1996) with no slip boundaries, the vertical velocity skewness for Rayleigh–Bénard convection is observed to be negative in the surface layer above the lower surface and correspondingly positive under the upper surface. The reasoning given is that the negative s_z at the lower surface is caused by plumes of cold, descending fluid that extend between the two surfaces, hitting the lower surface with localized negative velocities (Kerr, 1996). Likewise positive s_z occurs at the upper boundary as rising plumes hit it. However, we see the opposite, positive skewness at the lower boundary and negative skewness near the upper boundary. This indicates that in our simulations the upwelling velocities at the lower boundary are stronger than the velocities of the sinking plumes as they hit the lower surface. An analogous situation occurs at the upper boundary. We believe this is a result of the free slip boundary condition, the high Rayleigh number, and our 2D geometry. In the inertial, anelastic cases we see large regions of negative s_z below the upper boundary as there are a multitude of

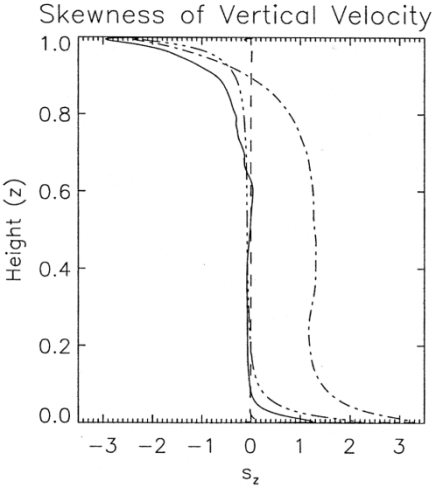

FIGURE 7 The skewness of the vertical velocity with depth is shown for anelastic with rotation and magnetic fields (solid line), Boussinesq with magnetic fields (dashed line), Boussinesq without inertial terms (dash triple dot line), and anelastic without inertial terms (dash single dot line).

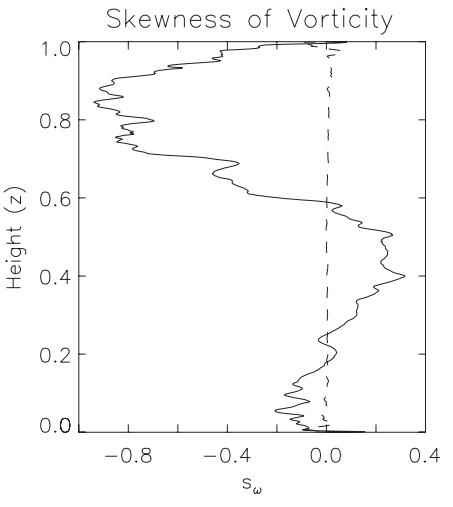

FIGURE 8 The skewness of the vorticity is shown for two sample cases: anelastic with rotation and magnetic fields (solid line) and Boussinesq without magnetic fields (dashed line). The anelastic case is influenced by Coriolis forces and shows major deviations from zero indicating additional vorticity generation caused by rotation and density stratification. The Boussinesq case, averaging zero, shows an even distribution of vorticity to either side of the mean vorticity.

small sinking plumes but no correspondingly concentrated upwelling because the large upwelling plume that dominates the convection in the lower, dense regions expands as it impinges upon the less dense regions converting much of its rising kinetic energy to horizontal kinetic energy. The noninertial case is again quite unique; rising plume velocities tend to be greater than sinking plume velocities over most of the region, resulting in a positive skewness in the vertical velocity everywhere but near the top boundary.

The sign of the vorticity, ω, of the fluid indicates the direction the fluid is spinning relative to the box, positive for clockwise rotation and negative for counter-clockwise rotation. All of our cases, except the rotating, magnetic anelastic case, have mean vorticities and vorticities skewness close to zero, as would be expected for these horizontally periodic solutions where there are two equally probable types of vorticity corresponding to clockwise and counter-clockwise circulations. Rotation however breaks this symmetry. With $\mathbf{\Omega}$ being in the $-y$ direction, Coriolis forces generate positive vorticity in rising, expanding plumes and negative vorticity in sinking, contracting plumes (Glatzmaier and Gilman, 1981). This produces a slight positive skewness of vorticity in the lower part of the box and negative skewness of vorticity in the upper part. This is illustrated in Fig. 8 where the vorticity skewness for the rotating anelastic case is compared with that for the nonrotating Boussinesq case, which has vorticity skewness close to zero at all depths, indicating symmetric distribution of positive and negative vorticity.

4 CONCLUSIONS

We have shown that the differences between anelastic and Boussinesq convection are readily apparent in the structure, distribution, and the abundance of thermal plumes.

In addition, the expansion and contraction of the fluid as its depth changes in the anelastic case allows Coriolis forces to play an important role in the generation of vorticity. Removing the influence of the magnetic field results in finer structure and greater fluid velocities. Neglecting the inertial terms results in artificially finer scale structures and a significantly different style of fluid motion for the anelastic fluid. A statistical comparison of these cases demonstrates significant differences between each of the approximations especially among the various anelastic cases.

We have considered a relatively high value of the Rayleigh number and investigated the effects of common approximations made when modeling convection. Rogers *et al.* (2003), using a similar 2D anelastic model, show how the Nusselt number and Reynolds number vary with the Rayleigh number for turbulent anelastic convection. However instead of specifying viscous and thermal diffusivities constant in z, as we do here, they specify constant dynamic viscosity ($\bar{\rho}\bar{\nu}$) and thermal conductivity ($C_p\bar{\rho}\bar{\kappa}$). This suppresses small scale sinking plumes at the top boundary.

Each of these approximations, neglecting density stratification, magnetic fields, or inertial terms, causes changes in the fluid behavior and therefore should be avoided when modeling the dynamics of the low viscosity, density-stratified, electrically-conducting fluid interiors of giant planets. However, the magnetic field appears to have the smallest effect on bulk fluid properties and, in a model of Jupiter, would not have a significant effect in the upper region where the electrical conductivity is relatively small. It would be interesting to see how density stratification and magnetic fields affect the dynamics seen in recent 3D global simulations of convection in Jupiter (Aurnou and Olson, 2001; Christensen, 2001, 2002; Wicht *et al.*, 2002).

Acknowledgments

Support was provided by NASA Planetary Atmospheres Program, NSF Geophysics Program, University of California Research Partnership Initiatives Program, and the Los Alamos Institute of Geophysics and Planetary Physics. Computing resources were provided by an NSF MRI funded Beowulf cluster at UCSC.

References

Aurnou, J.M. and Olson, P.L., "Strong zonal winds from thermal convection in a rotating spherical shell", *Geophys. Research Lett.* **28**, 2557–2559 (2001).

Braginsky, S.I. and Roberts, P.H., "Equations governing Earth's core and the geodynamo", *Astrophys. Fluid Dynam.* **79**, 1–97 (1995).

Bunge, H.-P., Richards, M.A. and Baumgardner, J.R., "Effect of depth-dependant viscosity on the planform of mantle convection", *Nature* **379**, 436–438 (1996).

Christensen, U.R., "Zonal flow driven by deep convection in major planets", *Geophys. Research Lett.* **28**, 13, 2553–2556 (2001).

Christensen, U.R., "Zonal flow driven by strongly supercritical convection in rotating spherical shells", *J. Fluid Mech.* **470**, 115–133 (2002).

DeLuca, E.E., Werne, J., Rosner, R. and Cattaneo, F., "Numerical simulations of soft and hard turbulence: preliminary results for two-dimension convection", *Phys. Rev. Lett.* **64**, 20, 2370–2373 (1990).

Glatzmaier, G.A. and Gilman, P.A., "Compressible convection in a rotating spherical shell. III Analytic model for compressible vorticity waves", *Astrophys. J.* **45**, 381–388 (1981).

Glatzmaier, G.A. and Roberts, P.H., "A three-dimensional convective dynamo solution with rotating and finitely conducting inner core and mantle", *Phys. Earth Planet. Inter.* **91**, 63–75 (1995).

Guillot, T., "A comparision of the interiors of Jupiter and Saturn", *Planet. Space Sci.* **47**, 1183–1200 (1999).

Heslot, F., Castaing, B. and Libchaber, A., "Transition to turbulence in helium gas", *Phys. Rev. A* **36**, 5870–5873 (1987).
Hubbard, W.B., *Planetary Interiors*, Van Nostrand-Reinhold, New York (1984).
Hurlburt, N.E., Toomre, J. and Massaguer, J.M., "Two-dimensional compressible convection extending over multiple scale heights", *Astrophys. J.* **282**, 557–573 (1984).
Julien, K., Legg, S., McWilliams, J. and Werne, J., "Rapidly rotating turbulent Rayleigh-Bénard convection", *J. Fluid Mech.* **322**, 243–273 (1996).
Kerr, R.M., "Rayleigh number scaling in numerical convection", *J. Fluid Mech.* **310**, 139–179 (1996).
Kuang, W. and Bloxham, J., "Numerical modeling of magnetohydrodynamic convection in a rapidly rotating spherical shell: weak and strong field dynamo action", *J. Comp. Phys.* **153**, 51–81 (1999).
Moeng, C.-H. and Rotunno, R., "Vertical-velocity skewness in the buoyancy-driven boundary layer", *Atmos. Sci.* **47**, 1149–1162 (1990).
Nellis, W.J., Weir, S.T. and Michell, A.C., "Metalization and electrical conductivity of Hydrogen in Jupiter", *Science* **273**, 936–938 (1996).
Rogers, T.M., Glatzmaier, G.A. and Woosley, S.E., "Simulations of two-dimensional turbulent convection in a density-stratified fluid", *Phys. Rev. E* **67**, 026315 (2003).
Sirovich, L., Balachandar, S. and Maxey, M.R., "Simulations of turbulent thermal convection", *Phys. Fluids A* **1**(12), 1911–1914 (1989).
Sun, Z., Schubert, G. and Glatzmaier, G.A., "Banded surface flow maintained by convection in a model of the rapidly rotating planets", *Science* **260**, 661–664 (1993).
Tackley, P.J., Stevenson, D.J., Glatzmaier, G.A. and Schubert, G., "Effects of an endothermic phase-transition at 670 km depth in a spherical model of convection in the earth's mantle", *Nature* **361**, 699–704 (1993).
Weiss, N.O., "Convection in an imposed magnetic field. Part 1. The development of nonlinear convection", *J. Fluid Mech.* **108**, 247–272 (1981a).
Weiss, N.O., "Convection in an imposed magnetic field. Part 2. The dynamical regime", *J. Fluid Mech.* **108**, 273–289 (1981b).
Wicht, J., Jones, C.A. and Zhang, K., "Instability of zonal flows in rotating spherical shells: an application to Jupiter", *Icarus* **155**, 425–435 (2002).